

FARIS: Fluid-Active-RIS

Hong-Bae Jeon, *Member, IEEE*

Abstract—In this paper, we introduce a fluid-active reconfigurable intelligent surface (FARIS) that combines fluid-based port repositioning with per-element active amplification to enhance the performance of 6G network. To characterize the performance, we formulate an ergodic-rate maximization problem that jointly optimizes both the active amplification-reflection vector and the discrete selection of fluid active elements under practical hardware constraints. The problem is addressed via an alternating optimization (AO) framework, which progressively improves the rate. Complexity and convergence analyses that follow furnish deeper insight into the algorithmic operation and performance enhancement. Numerical results confirm that the proposed FARIS with AO framework consistently outperforms conventional FRIS/ARIS, delivering higher rates across diverse environments, often even when using fewer active elements or a smaller physical aperture.

Index Terms—Fluid active reconfigurable intelligent surface (FARIS), ergodic rate, alternating optimization.

I. INTRODUCTION

RECENTLY, reconfigurable intelligent surfaces (RISs) have emerged as a key technology for sixth-generation (6G) wireless networks, primarily due to their capability to passively reconfigure the radio environment with minimal power consumption [1], [2]. An RIS typically comprises a large array of programmable, low-cost metasurface elements whose tunable reflection characteristics enable fine-grained manipulation of electromagnetic waves [3]. By coordinating the phase shifts across these elements, RISs can intentionally steer, focus, or scatter incident signals, thereby improving coverage, link reliability, spectral efficiency, and even localization performance across diverse wireless scenarios [4], [5]. Although RIS is recognized for its cost- and energy-efficiency in boosting wireless coverage and capacity, its practical deployment remains challenging. One critical issue is that since conventional RIS architectures rely solely on passive reflecting elements, it inevitably suffers from severe multiplicative fading, as their end-to-end path loss (PL) is the product of the Tx-RIS and RIS-Rx channel losses. This fundamental limitation significantly degrades performance in practical deployments [6], [7].

To address this fundamental physical bottleneck, recent research has introduced active-RIS (ARIS) as a new architecture for wireless communication systems [8], [9]. Unlike conventional passive-RIS (PRIS) that merely reflects incident signals, ARIS incorporates reflection-type amplifiers into their elements, enabling them to amplify the reflected signals. Although this requires additional power consumption,

This work was supported by Hankuk University of Foreign Studies Research Fund of 2025. (Corresponding Author: Hong-Bae Jeon.)

H.-B. Jeon is with the Department of Information Communications Engineering, Hankuk University of Foreign Studies, Yong-in, 17035, Korea (e-mail: hongbae08@hufs.ac.kr).

the resulting gain can effectively compensate for the severe double-reflection path loss, making ARIS a promising solution to the “multiplicative fading” problem. Several studies have further demonstrated the performance gains of ARIS in various wireless settings, including joint beamforming optimization with sub-connected architectures [10], signal-to-noise-ratio (SNR)-oriented analyses under identical power budget with PRIS [11], [12], and average sum-rate maximization [13] and power-minimizing [14] frameworks under partial channel-state-information (CSI) conditions, highlighting its potential to fundamentally enhance coverage, reliability, and spectral efficiency.

Another critical issue is that conventional RIS architectures rely on a fixed and finitely quantized phase-control structure, which fundamentally limits their ability to realize the truly smart and highly adaptive wireless environment they were originally envisioned for [15]. As a result, practical RIS implementations often fall short of achieving environment-level reconfigurability, undermining the very motivation of deploying low-cost surfaces to offload complexity from base stations (BSs) [16]. Furthermore, this fixed structure is also unfavorable for achieving high degree-of-freedom (DoF) in RIS-aided channels [17], [18], as substantial DoF gains generally necessitate scaling up the RIS [19]–[21], inevitably leading to increased training overhead and greater implementation complexity [22], [23]. Thus, the rigid structure of conventional RIS not only limits its adaptability to smart environments but also fundamentally restricts scalable DoF enhancement, which additionally limits its ability to effectively mitigate the aforementioned multiplicative-fading effect.

In this context, the concept of fluid antenna system (FAS) has emerged as a compelling solution [24], [25]. Unlike conventional fixed-structure antennas, FAS offers shape- and position-reconfigurability enabled by flexible materials and architectures [26], [27], thereby introducing additional physical-layer DoFs that can be exploited for performance enhancement [28]. Since the FAS is first introduced [24], several studies have been made to understand the various performance limits of FAS [28]–[30], enable channel estimation schemes for FAS [31]–[33], and apply with several other applications including RIS [34], [35], integrated-sensing-and-communications (ISAC) [36], [37], and direction-of-arrival (DoA) estimations [38], [39]. Taken together, these studies establish FAS as a promising paradigm that surpasses conventional antenna systems by unlocking higher spatial diversity, and by offering a versatile platform that can be seamlessly integrated into diverse 6G wireless functionalities.

Inspired by the position-reconfigurability of FAS, recent work has extended this concept to RIS through the notion of fluid-RIS (FRIS) [40], [41], where the RIS hosts a movable “fluid” elements capable of dynamically changing its posi-

tion and applying optimized phase shifts [42]. By allowing a small number of mobile elements to traverse a larger physical aperture, FRIS effectively extracts spatial-domain DoFs without increasing the number of reflecting units [43], offering a fundamentally different path toward scalable DoF enhancement under practical hardware constraints [44]. While FRIS achieves meaningful performance gains through spatial-domain mobility, its reliance on passive reflection still leaves substantial headroom for further enhancement.

This naturally raises the question of whether combining FRIS with the signal-amplification capability of ARIS could unlock even greater benefits. Importantly, however, our proposed architecture is not a mere system-level stacking of ARIS and FRIS mechanisms. Rather, it introduces a fundamentally new form of metasurface in which each active reflecting element functions as a fluidic unit, capable of providing controllable amplification while dynamically repositioning within its assigned subregion. In other words, this fluid-active behavior is intrinsically integrated into the surface itself.

In particular, we introduce fluid-active-RIS (FARIS), a novel paradigm that integrates the signal-amplification functionality of ARIS with the spatial reconfigurability of FRIS. Unlike FRIS and static ARIS, FARIS equips the surface with a fluidic-active-element that can simultaneously amplify and reflect incoming signals while freely adjusting its position within a predefined aperture. This dual capability allows the surface to adapt its spatial energy distribution in real time, thereby enabling (i) position-adaptive spatial-DoF extraction and (ii) compensation of multiplicative fading through active gain. As a result, FARIS achieves a fundamentally stronger form of environment control, offering a powerful and versatile platform for 6G wireless network.

The main contributions are summarized as follows:

- 1) We introduce the FARIS framework for a downlink setting and develop a unified formulation for joint port selection and amplification-phase design. By explicitly modeling the spatial correlation among activated FARIS ports and incorporating a practical ARIS reflection-power constraint, we cast an ergodic-rate maximization problem that simultaneously optimizes the amplification-reflection vector and the discrete configuration of fluid-reconfigurable ports.
- 2) To address the mixed-integer non-convex nature of the problem, we develop an alternating-optimization (AO) framework for design on FARIS architecture. With the port configuration fixed, we employ sample average approximation (SAA) together with a quadratic fractional transform to convert the objective into a sequence of convex conic subproblems in a lifted matrix variable. When the resulting solution is not rank-one, Gaussian randomization and magnitude projection are applied. We additionally establish that this inner-loop procedure guarantees monotonic improvement of the SAA objective and convergence to a stationary point.
- 3) For discrete port selection under a cardinality constraint on the activable FARIS elements, given the current amplification-reflection vector, we propose a cardinality-constrained cross-entropy method (CEM) that draws

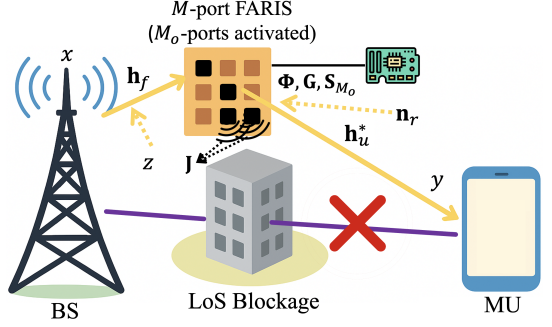


Fig. 1. System model of FARIS-aided wireless network.

Bernoulli activation samples and updates an independent Bernoulli distribution to fit the statistics of the high-rate elite subset. We derive a closed-form CEM update, showing that the optimal activation probabilities are parametrized by a single Lagrange multiplier and that the resulting mapping admits a unique solution enforcing the cardinality budget. The smoothed update is proven to monotonically increase the empirical log-likelihood, and yields a non-decreasing sequence of ergodic rates.

- 4) Building on these, we integrate the active-reflection design and the port selection into a unified AO framework. We prove that each outer iteration produces a non-decreasing ergodic-rate sequence by leveraging the monotonicity of both the lifted conic subproblem and the likelihood-improving CEM update. Consequently, the overall AO procedure is guaranteed to converge to a finite limit, providing a principled mechanism for jointly optimizing continuous amplification-phase variables and discrete fluid-port configurations. We conduct a detailed complexity analysis of each algorithmic block, where the resulting expressions characterize how the overall computational cost scales, thereby confirming the polynomial-time implementability of the FARIS with proposed AO framework.
- 5) Extensive Monte-Carlo simulations are performed over a wide range of system parameters, including transmit power, total number of FARIS elements, and normalized aperture. The results show that the proposed FARIS architecture with AO framework exhibits fast convergence within a modest number of outer AO iterations and achieves near-optimal ergodic rate with only marginal loss compared to brute-force search (BFS), while drastically reducing computational burden. Moreover, FARIS consistently outperforms conventional FRIS and ARIS baselines, achieving significantly higher rates even with fewer active elements or smaller apertures.

To the best of our knowledge, this is the first work to propose a new paradigm that tightly integrates fluid port repositioning with ARIS, complemented by analytical and numerical complexity analyses and extensive simulations demonstrating its near-optimality and clear performance advantages over benchmarks.

II. SYSTEM MODEL

As illustrated in Fig. 1, we examine a downlink wireless system assisted by FARIS. A BS equipped with a single fixed-position antenna (FPA) communicates with a mobile user (MU), also equipped with a single FPA, through the FARIS. The direct BS-MU link is assumed to be completely blocked by obstacles such as buildings. The FARIS consists of $M = M_x \times M_x$ reflective elements arranged over a surface of size $W_x \lambda \times W_x \lambda$, where λ denotes the carrier wavelength and W_x represents the normalized aperture of the FARIS relative to λ . The inter-element spacing is $d = \frac{W_x \lambda}{M_x}$, resulting in a spatial correlation matrix $\mathbf{J} \triangleq [J_{ij}] \in \mathbb{R}^{M \times M}$ modeled according to Jakes' model. The spatial correlation between the i th and j th elements is given by [43], [44]

$$J_{ij} = j_0 \left(\frac{2\pi d_{ij}}{\lambda} \right), \quad (1)$$

where $j_0(\cdot)$ denotes the zero-order spherical Bessel function of the first kind, and $d_{ij} = d\sqrt{(\text{mod}(i, M_x) - \text{mod}(j, M_x))^2 + \left(\left\lfloor \frac{i}{M_x} \right\rfloor - \left\lfloor \frac{j}{M_x} \right\rfloor\right)^2}$ is the distance between the i and j th elements. Following [44] and differing from [40], each FARIS element can be viewed as a port of a fluid antenna structure. Each element operates in one of two states: “on” and “off”. In the “on” state, the element actively interacts with incoming electromagnetic waves, modifying their amplitude and phase to realize the desired reflection. In the “off” state, the element is terminated by a matched load, effectively isolating it from the impinging wave and preventing any alteration of the signal.

The BS-FARIS link is assumed line-of-sight (LoS); $\tilde{\mathbf{h}}_f \in \mathbb{C}^M$, where as noted in [45], it occurs when the BS-FARIS distance is shorter than the advanced MIMO Rayleigh distance (MIMO-ARD), represented as $D^{\text{RB}} \triangleq \lambda M$. The FARIS-MU link experiences Rician fading:

$$\mathbf{h}_u = \sqrt{\frac{K}{K+1}} \tilde{\mathbf{h}}_u + \sqrt{\frac{1}{K+1}} \hat{\mathbf{h}}_u \in \mathbb{C}^{M \times 1}, \quad (2)$$

where $\tilde{\mathbf{h}}_u$ and $\hat{\mathbf{h}}_u \sim \mathcal{CN}(0, \mathbf{I}_M)$ are the deterministic LoS and the non-LoS (NLoS) component, respectively, where \mathbf{I}_M is an $M \times M$ identity matrix.

Out of the total M candidate ports, only M_o are activated. This selection process is represented as

$$\mathbf{S}_{M_o}^T \triangleq [\mathbf{e}_{i_1} \cdots \mathbf{e}_{i_{M_o}}] \in \mathbb{R}^{M \times M_o} \quad (\forall i_n \in \{1, \dots, M\}), \quad (3)$$

where \mathbf{e}_i denotes the i th canonical basis vector (i.e., the i th column of \mathbf{I}_M). This construction implies that only the ports indexed by $\{i_n\}_{n=1}^{M_o}$ are active on the FARIS. To ensure unique activation, all columns of $\mathbf{S}_{M_o}^T$ must be mutually distinct, preventing redundant port selection.

The functionality of \mathbf{S}_{M_o} -utilized FARIS ports can be represented by a phase-shift Φ and amplifier matrix \mathbf{G} :

$$\begin{aligned} \Phi &= \text{diag}(e^{j\phi_1}, \dots, e^{j\phi_{M_o}}) \quad (\forall \phi_i \in [0, 2\pi]), \\ \mathbf{G} &= \text{diag}(g_1, \dots, g_{M_o}) \quad (\forall g_i \in [0, g_{\max}]). \end{aligned} \quad (4)$$

The effective operator \mathbf{A}_{act} of FARIS is therefore

$$\mathbf{A}_{\text{act}} \triangleq \mathbf{J}^{\frac{1}{2}} \mathbf{S}_{M_o}^T \text{diag}(\mathbf{v}) \mathbf{S}_{M_o} \mathbf{J}^{\frac{1}{2}}, \quad (5)$$

where

$$\mathbf{v} = [v_1 \cdots v_{M_o}]^T, \quad v_i = g_i e^{j\phi_i} \leftrightarrow \text{diag}(\mathbf{v}) = \Phi \mathbf{G} \quad (6)$$

denotes the concatenated amplification ($\{g_i\}$) and reflection ($\{\phi_i\}$) mechanism on FARIS, where the magnitude and phase of v_i correspond each, respectively.

The BS transmits a unit-power symbol x with power P , and noise at the FARIS and the MU are respectively given by $\mathbf{n}_r \sim \mathcal{CN}(\mathbf{0}, \sigma_r^2 \mathbf{I}_M)$, $z \sim \mathcal{CN}(0, \sigma_0^2)$. In summary, the signal \mathbf{s}_{RIS} radiated by FARIS is

$$\mathbf{s}_{\text{RIS}} = \mathbf{A}_{\text{act}} \left(\sqrt{PL_f} \tilde{\mathbf{h}}_f x + \mathbf{n}_r \right), \quad (7)$$

where L_f is the PL of the BS-FARIS link. The instantaneous radiated power P_{RIS} at FARIS is therefore

$$P_{\text{RIS}} = PL_f \|\mathbf{A}_{\text{act}} \tilde{\mathbf{h}}_f\|_2^2 + \sigma_r^2 \text{tr}(\mathbf{A}_{\text{act}} \mathbf{A}_{\text{act}}^*), \quad (8)$$

and with the power budget P_{\max} , the hardware constraint is

$$P_{\text{RIS}} \leq P_{\max}. \quad (9)$$

The received signal y at MU is

$$\begin{aligned} y &= \sqrt{L_u} \mathbf{h}_u^* \mathbf{s}_{\text{RIS}} + z \\ &= \sqrt{PL_f L_u} \mathbf{h}_u^* \mathbf{A}_{\text{act}} \tilde{\mathbf{h}}_f x + \sqrt{L_u} \mathbf{h}_u^* \mathbf{A}_{\text{act}} \mathbf{n}_r + z, \end{aligned} \quad (10)$$

where L_u denotes the PL of the FARIS-MU link. From (10), the instantaneous signal-to-interference-noise-ratio (SINR) is

$$\gamma = \frac{PL_f L_u |\mathbf{h}_u^* \mathbf{A}_{\text{act}} \tilde{\mathbf{h}}_f|^2}{\sigma_0^2 + \mathbf{h}_u^* \mathbf{B} \mathbf{h}_u}, \quad (11)$$

where $\mathbf{B} \triangleq L_u \sigma_r^2 \mathbf{A}_{\text{act}} \mathbf{A}_{\text{act}}^*$, and the ergodic rate \bar{R} is

$$\bar{R} \triangleq \mathbb{E}_{\mathbf{h}_u} [\log_2(1 + \gamma)]. \quad (12)$$

Hence, the overall design problem of the FARIS-enabled system can be formulated as

$$\max_{\mathbf{v}, \mathbf{S}_{M_o}} \bar{R} \text{ s.t. (9), } \forall |v_i| \leq g_{\max}, \quad \mathbf{S}_{M_o} \in \{0, 1\}^{M_o \times M}. \quad (13)$$

Note that since $\text{diag}(\mathbf{v}) = \Phi \mathbf{G}$, we solve (13) and decompose $\{v_i\}$ into magnitude and phase, which corresponds to $\{g_i\}$ and $\{e^{j\phi_i}\}$ ($\leftrightarrow \{\phi_i\}$), respectively.

III. ALTERNATING OPTIMIZATION FRAMEWORK

To jointly optimize $\mathbf{v} (\leftrightarrow (\Phi, \mathbf{G}))$ and \mathbf{S}_{M_o} , we adopt an AO approach.

A. Optimizing $\mathbf{v} (\leftrightarrow (\Phi, \mathbf{G}))$ for Fixed \mathbf{S}_{M_o}

When \mathbf{S}_{M_o} is fixed, define the lifted variable \mathbf{V} as

$$\mathbf{V} \triangleq \mathbf{v} \mathbf{v}^* \succeq \mathbf{0} \quad (\text{rank} \mathbf{V} = 1). \quad (14)$$

We approximate (12) via the SAA using S independent and identically distributed (i.i.d.) samples $\{\mathbf{h}^{(s)}\}_{s=1}^S$ of \mathbf{h}_u :

$$\bar{R}_S \triangleq \frac{1}{S} \sum_{s=1}^S \log_2 \left(1 + \underbrace{\frac{PL_f L_u |\mathbf{h}^{(s)*} \mathbf{A}_{\text{act}} \tilde{\mathbf{h}}_f|^2}{\sigma_0^2 + \mathbf{h}^{(s)*} \mathbf{B} \mathbf{h}^{(s)}}}_{\triangleq \gamma_s} \right). \quad (15)$$

To transform the problem with respect to \mathbf{V} , we introduce the following theorem:

Theorem 1. Define

$$\mathbf{b} \triangleq \mathbf{S}_{M_o} \mathbf{J}^{\frac{1}{2}} \tilde{\mathbf{h}}_f, \quad \mathbf{u}_s \triangleq \mathbf{S}_{M_o} \mathbf{J}^{\frac{1}{2}} \mathbf{h}^{(s)}, \quad \mathbf{K} \triangleq \mathbf{S}_{M_o} \mathbf{J} \mathbf{S}_{M_o}^T, \quad (16)$$

and

$$\mathbf{a}_s \triangleq \mathbf{u}_s \odot \bar{\mathbf{b}}, \quad \mathbf{C}_s \triangleq L_u \sigma_r^2 (\mathbf{K} \odot (\mathbf{u}_s \mathbf{u}_s^*)), \quad (17)$$

where $\bar{\mathbf{b}}$ is the element-wise conjugate of \mathbf{b} . Then the following hold:

- γ_s can be written as

$$\gamma_s = \frac{PL_f L_u \mathbf{v}^* \mathbf{a}_s \mathbf{a}_s^* \mathbf{v}}{\sigma_0^2 + \mathbf{v}^* \mathbf{C}_s \mathbf{v}} = \frac{PL_f L_u \text{tr}(\mathbf{a}_s \mathbf{a}_s^* \mathbf{V})}{\sigma_0^2 + \text{tr}(\mathbf{C}_s \mathbf{V})}. \quad (18)$$

- P_{RIS} satisfies

$$P_{\text{RIS}} = \mathbf{v}^* (PL_f \mathbf{Q}_1 + \sigma_r^2 \mathbf{Q}_2) \mathbf{v} = \text{tr}(\mathbf{F} \mathbf{V}), \quad (19)$$

where $\mathbf{F} \triangleq PL_f \mathbf{Q}_1 + \sigma_r^2 \mathbf{Q}_2$ and

$$\mathbf{Q}_1 \triangleq \text{diag}(\mathbf{b}^*) \mathbf{K} \text{diag}(\mathbf{b}) = \mathbf{K} \odot (\bar{\mathbf{b}} \mathbf{b}^T), \quad \mathbf{Q}_2 \triangleq \mathbf{K} \odot \mathbf{K}. \quad (20)$$

Proof. See Appendix A. \blacksquare

Hence by Theorem 1, the active reflection design subproblem becomes

$$\begin{aligned} & \max_{\mathbf{V}} \frac{1}{S} \sum_{s=1}^S \log_2 \left(1 + \frac{PL_f L_u \text{tr}(\mathbf{a}_s \mathbf{a}_s^* \mathbf{V})}{\sigma_0^2 + \text{tr}(\mathbf{C}_s \mathbf{V})} \right) \\ & \text{s.t. } \text{tr}(\mathbf{F} \mathbf{V}) \leq P_{\text{max}}, \quad V_{ii} \leq g_{\text{max}}^2 \quad (i = 1, \dots, M_o), \\ & \quad \text{rank} \mathbf{V} = 1, \quad \mathbf{V} \succeq 0, \end{aligned} \quad (21)$$

where V_{ii} is the ii th component of \mathbf{V} . Problem (21) is still not convex due to the fractional objective and the rank-1 constraint. To handle the nonconvex fractional structure, we will drop the rank constraint and apply a fractional/quadratic transform to obtain a sequence of convex conic subproblems in \mathbf{V} , followed by Gaussian randomization [46] and magnitude projection if necessary.

We first apply the quadratic transform, also known as the fractional programming technique, to (21). For each s , introduce an auxiliary variable $y_s \geq 0$ and use the following transformation for $A \geq 0$ and $B > 0$ [47]:

$$\frac{A}{B} = \max_{y \geq 0} (2y\sqrt{A} - y^2 B), \quad (22)$$

where the unique maximizer is given by $y^* = \frac{\sqrt{A}}{B}$. Equation (22) converts a ratio into a concave quadratic form with respect to $y \geq 0$ and yields a closed-form update for y given the other variables, enabling alternating optimization for sum-of-log-fraction objectives. Applying the result to (18), (15) is equivalently lower-bounded as

$$\begin{aligned} \bar{R}_S & \geq \frac{1}{S} \sum_{s=1}^S \log_2 (1 + \xi_s), \\ \xi_s & \triangleq PL_f L_u \left(2y_s \sqrt{\text{tr}(\mathbf{a}_s \mathbf{a}_s^* \mathbf{V})} - y_s^2 (\sigma_0^2 + \text{tr}(\mathbf{C}_s \mathbf{V})) \right) (\geq 0), \end{aligned} \quad (23)$$

where the maximum $\xi_s = \gamma_s$ holds by substituting $y_s = \frac{\sqrt{\text{tr}(\mathbf{a}_s \mathbf{a}_s^* \mathbf{V})}}{\sigma_0^2 + \text{tr}(\mathbf{C}_s \mathbf{V})}$. We will therefore maximize $\frac{1}{S} \sum_{s=1}^S \log_2 (1 + \xi_s)$

as the lower-bound of objective in (21), which is constructed by the following procedure:

1) *Update of \mathbf{V} ($\leftrightarrow \mathbf{v}$) for fixed $\{y_s\}$:* Since $\sqrt{\text{tr}(\mathbf{a}_s \mathbf{a}_s^* \mathbf{V})}$ in (23) is nonconvex with respect to \mathbf{V} , by introducing the slack variables $\{w_s \geq 0\}_{s=1}^S$, $\sqrt{\text{tr}(\mathbf{a}_s \mathbf{a}_s^* \mathbf{V})}$ is handled by w_s subject to the second-order cone (SOC) \mathcal{Q}_r [48]:

$$\left(w_s, \sqrt{\text{tr}(\mathbf{a}_s \mathbf{a}_s^* \mathbf{V})} \right) \in \mathcal{Q}_r \Leftrightarrow w_s \leq \sqrt{\text{tr}(\mathbf{a}_s \mathbf{a}_s^* \mathbf{V})}, \quad (24)$$

which is equivalent to stating that w_s forms the hypograph of $\sqrt{\text{tr}(\mathbf{a}_s \mathbf{a}_s^* \mathbf{V})}$. Hence, for fixed $\{y_s\}$, the transformed subproblem becomes

$$\begin{aligned} & \max_{\mathbf{V}, \{w_s, \xi_s\}} \frac{1}{S} \sum_{s=1}^S \log_2 (1 + \xi_s) \\ & \text{s.t. } \xi_s \leq PL_f L_u (2y_s w_s - y_s^2 (\sigma_0^2 + \text{tr}(\mathbf{C}_s \mathbf{V}))), \\ & \quad \left(w_s, \sqrt{\text{tr}(\mathbf{a}_s \mathbf{a}_s^* \mathbf{V})} \right) \in \mathcal{Q}_r, \\ & \quad w_s \geq 0, \quad \xi_s \geq 0, \quad \mathbf{V} \succeq 0, \\ & \quad \text{tr}(\mathbf{F} \mathbf{V}) \leq P_{\text{max}}, \quad V_{ii} \leq g_{\text{max}}^2, \\ & \quad (i = 1, \dots, M_o, \quad s = 1, \dots, S). \end{aligned} \quad (25)$$

Problem (25) is a convex conic optimization problem with linear matrix inequality (LMI) and SOC constraints. Upon solving it, if the optimal \mathbf{V}_0 is rank-one, the corresponding \mathbf{v}_0 is directly obtained as its principal eigenvector satisfying $\mathbf{V}_0 = \mathbf{v}_0 \mathbf{v}_0^*$. Otherwise, \mathbf{v}_0 is extracted via Gaussian randomization, starting by computing the Cholesky factorization of \mathbf{V}_0 : $\mathbf{V}_0 = \mathbf{L} \mathbf{L}^*$ [49], where \mathbf{L} is a lower-triangular matrix. We then generate N_{rand} independent Gaussian realizations:

$$\mathbf{v}_n = \mathbf{L} \mathbf{z}_n \quad (n = 1, \dots, N_{\text{rand}}), \quad (26)$$

where $\{\mathbf{z}_n \sim \mathcal{CN}(\mathbf{0}, \mathbf{I}_{M_o})\}$ are i.i.d. standard circularly symmetric complex Gaussian random vectors. For each \mathbf{v}_n , we form the rank-one matrix $\mathbf{V}_n \triangleq \mathbf{v}_n \mathbf{v}_n^*$, and solve (25) with \mathbf{V} replaced by fixed \mathbf{V}_n , which is convex in $\{w_s, \xi_s\}$. Let the optimum be

$$\tilde{R}_n \triangleq \frac{1}{S} \sum_{s=1}^S \log_2 (1 + \xi_s^{[n]}), \quad (27)$$

where $\xi_s^{[n]}$ is the optimizer with respect to ξ_s . We then select the best randomized sample index as

$$n^* = \arg \max_{n \in \{1, \dots, N_{\text{rand}}\}} \tilde{R}_n. \quad (28)$$

We then enforce \mathbf{v}_{n^*} (or \mathbf{v}_0) by element-wise magnitude projection onto $[0, g_{\text{max}}]$ to ensure feasibility [46]:

$$\forall v'_i \leftarrow \min\{g_{\text{max}}, |v'_i|\} e^{j \angle v'_i}, \quad (29)$$

where v'_i is the i th component of corresponding \mathbf{v}_{n^*} or \mathbf{v}_0 .

2) *Update of y_s for fixed \mathbf{V} :* For fixed \mathbf{V} , each y_s admits the closed-form update

$$y_s^* = \frac{w_s}{\sigma_0^2 + \text{tr}(\mathbf{C}_s \mathbf{V})} \quad (s = 1, \dots, S). \quad (30)$$

By alternately updating \mathbf{V} from (25) and $\{y_s\}$ from (30), the objective is guaranteed to be non-decreasing until convergence, which will be shown later. The overall procedure is given by

Algorithm 1 AO Framework of \mathbf{v} and $\{y_s\}$ for Fixed \mathbf{S}_{M_o}

```

1: Input:  $\{\mathbf{h}^{(s)}\}_{s=1}^S$ ,  $\epsilon_v$ ,  $\mathbf{S}_{M_o}$ 
2: Initialize:  $\mathbf{v}^{[0]} (\leftrightarrow \mathbf{V}^{[0]})$  satisfying (9) and  $\forall |v_i^{[0]}| < g_{\max}$ ,  $\{y_s^{[0]}\}$ ,  $t \leftarrow 0$ 
3: Evaluate  $\bar{R}_S^{[0]}$  by (15)
4: repeat
5:   Solve (25) to obtain  $\mathbf{V}^{[t+1]}$ 
6:   if  $\text{rank} \mathbf{V}^{[t+1]} > 1$  then
7:     Extract  $\mathbf{v}^{[t+1]}$  via Gaussian randomization
8:     Project the magnitude of each element of  $\mathbf{v}^{[t+1]}$  onto  $[0, g_{\max}]$ 
9:   else
10:     $\mathbf{v}^{[t+1]} \leftarrow$  principal eigenvector of  $\mathbf{V}^{[t+1]}$ 
11:   end if
12:   for  $s = 1, \dots, S$  do
13:     Update  $y_s^{[t+1]}$  via (30) using  $\mathbf{V}^{[t+1]}$ 
14:   end for
15:   Evaluate  $\bar{R}_S^{[t+1]}$  by (15)
16:    $t \leftarrow t + 1$ 
17: until  $|\bar{R}_S^{[t]} - \bar{R}_S^{[t-1]}| < \epsilon_v$ 
18:  $\mathbf{v}^{\dagger} \leftarrow \mathbf{v}^{[t]} (\leftrightarrow \mathbf{V}^{\dagger} \leftarrow \mathbf{V}^{[t]})$ 
19: Output:  $\mathbf{v}^{\dagger} (\leftrightarrow \mathbf{V}^{\dagger})$ 

```

Algorithm 1.

Remark 1. In Algorithm 1, we initialize $\mathbf{v}^{[0]} (\leftrightarrow \mathbf{V}^{[0]})$ by drawing i.i.d. $\theta_i \sim \mathcal{U}[0, 2\pi]$, set $\bar{\mathbf{v}} = g_{\max}[e^{j\theta_1}, \dots, e^{j\theta_{M_o}}]^T$, and scale $\bar{\mathbf{v}} \rightarrow \mathbf{v}^{[0]}$ so that $\mathbf{v}^{[0]*} \mathbf{F} \mathbf{v}^{[0]} \leq P_{\max}$. This guarantees feasibility of (9) and $\forall |v_i^{[0]}| \leq g_{\max}$. Thereafter, we set $y_s^{[0]} = \frac{\sqrt{\text{tr}(\mathbf{a}_s \mathbf{a}_s^* \mathbf{V}^{[0]})}}{\sigma_0^2 + \text{tr}(\mathbf{C}_s \mathbf{V}^{[0]})}$ ($\forall s$).

3) *Monotonicity and Convergence Analysis of Algorithm 1:* To ensure that Algorithm 1 produces stable performance improvements, it is essential to verify that each iteration does not degrade \bar{R}_S . The following theorem establishes this monotonicity property.

Theorem 2. *In Algorithm 1, $\{\bar{R}_S^{[t]}\}$ monotonically non-decreases.*

Proof. See Appendix B. ■

Furthermore, since the feasible set of \mathbf{V} is compact due to the constraints $\text{tr}(\mathbf{F} \mathbf{V}) \leq P_{\max}$ and $V_{ii} \leq g_{\max}^2$ ($i = 1, \dots, M_o$) in (21), $\{\bar{R}_S^{[t]}\}$ is bounded above. Therefore, $\{\bar{R}_S^{[t]}\}_{t \geq 0}$ converges to a finite limit.

B. Optimizing \mathbf{S}_{M_o} for fixed \mathbf{v}

To stochastically determine the active ports for given \mathbf{v} , each port i is assigned an activation probability $p_i \in [0, 1]$, forming the probability vector $\mathbf{p} = [p_1 \dots p_M]^T$. Let $\zeta = [\zeta_1 \dots \zeta_M]^T \in \{0, 1\}^M$ denote a random binary port-activation vector sampled as

$$\zeta \sim \text{Bernoulli}(\mathbf{p}), \quad \mathbb{P}(\zeta; \mathbf{p}) = \prod_{i=1}^M p_i^{\zeta_i} (1 - p_i)^{1 - \zeta_i}. \quad (31)$$

We propose to utilize an M_o -constrained CEM that fits an independent Bernoulli law $\zeta \sim \text{Bernoulli}(\mathbf{p})$ to the elite set

of high-performing port subsets while exactly enforcing the expected-cardinality budget $\sum_{i=1}^M p_i = M_o$ [42], [44], [50].

1) *Ideal Target Distribution:* Let $\mathcal{Z} \subseteq \{0, 1\}^M$ denote the set of all feasible binary port-activation vectors, and let $\bar{R}_S(\zeta)$ be the objective in (15) corresponding to $\zeta \in \mathcal{Z}$. Define the elite threshold γ_ρ as the $(1 - \rho)$ -quantile of $\bar{R}_S(\zeta)$ under the current sampling distribution, so that a fraction ρ of samples satisfy $\bar{R}_S(\zeta) \geq \gamma_\rho$. The ideal target distribution $\mathbb{P}^\dagger(\zeta)$ that perfectly concentrates on the elite set is then

$$\mathbb{P}^\dagger(\zeta) \propto \begin{cases} 1 & (\bar{R}_S(\zeta) \geq \gamma_\rho) \\ 0 & (\text{otherwise}). \end{cases} \quad (32)$$

Intuitively, \mathbb{P}^\dagger assigns nonzero probability only to high-performing (elite) activation patterns.

The CEM seeks $\mathbb{P}(\zeta; \mathbf{p})$ that approximates \mathbb{P}^\dagger as closely as possible. Formally, this is achieved by minimizing the Kullback-Leibler (KL) divergence:

$$\begin{aligned} \mathbf{p}^{\text{new}} &\triangleq \arg \min_{\mathbf{p}} D_{\text{KL}}(\mathbb{P}^\dagger \parallel \mathbb{P}(\cdot; \mathbf{p})) \\ &= \arg \max_{\mathbf{p}} \mathbb{E}_{\mathbb{P}^\dagger} [\log \mathbb{P}(\zeta; \mathbf{p})]. \end{aligned} \quad (33)$$

Since \mathbb{P}^\dagger is unknown, we approximate the expectation in (33) using the empirical distribution of the elite samples:

$$\mathbb{E}_{\mathbb{P}^\dagger} [\log \mathbb{P}(\zeta; \mathbf{p})] \approx \frac{1}{N_e} \sum_{n \in \mathcal{E}} \log \mathbb{P}(\zeta_n; \mathbf{p}), \quad (34)$$

where we draw N_{mc} i.i.d. samples $\{\zeta_n\}_{n=1}^{N_{\text{mc}}}$ from Bernoulli(\mathbf{p}) and evaluate $\{\bar{R}_S(\zeta_n)\}_{n=1}^{N_{\text{mc}}}$. Let \mathcal{E} be the elite index set of the top- ρ fraction, with size of $N_e = \lceil \rho N_{\text{mc}} \rceil$ by definition. Maximizing (34) yields

$$\mathbf{p}^{\text{new}} = \arg \max_{\mathbf{p} \in [0, 1]^M} \frac{1}{N_e} \sum_{n \in \mathcal{E}} \log \mathbb{P}(\zeta_n; \mathbf{p}). \quad (35)$$

which is exactly the empirical log-likelihood maximization used in the CEM update rule.

2) *Applying to M_o -constrained CEM with Iterations:* We now modify the CEM with the aforementioned cardinality budget. Herein at iteration t , draw N_{mc} i.i.d. samples $\{\zeta_n^{[t]}\}_{n=1}^{N_{\text{mc}}}$ from Bernoulli($\mathbf{p}^{[t]}$) and evaluate $\{\bar{R}_S(\zeta_n^{[t]})\}_{n=1}^{N_{\text{mc}}}$. Let $\mathcal{E}^{[t]}$ be the elite index set of the top- ρ fraction, with size of $N_e = \lceil \rho N_{\text{mc}} \rceil$ by definition. Then we can define the elite empirical average per coordinate i :

$$\mu_i^{[t]} \triangleq \frac{1}{N_e} \sum_{n \in \mathcal{E}^{[t]}} \zeta_{n,i}^{[t]}, \quad (36)$$

where $\zeta_{n,i}^{[t]}$ is the i th component of $\zeta_n^{[t]}$ ($i = 1, \dots, M$). By substituting into (35), it becomes

$$\begin{aligned} \max_{\mathbf{p}} \Phi(\mathbf{p}) &\triangleq \sum_{i=1}^M \left(\mu_i^{[t]} \log p_i + (1 - \mu_i^{[t]}) \log(1 - p_i) \right) \\ \text{s.t. } &\sum_{i=1}^M p_i = M_o, \quad \mathbf{p} \in (0, 1)^M. \end{aligned} \quad (37)$$

Problem (37) is strictly concave with an affine constraint, hence admits a unique global maximizer, as characterized in the following theorem.

Algorithm 2 CEM-Based Selection of \mathbf{S}_{M_o} with Expected M_o -Cardinality for Fixed \mathbf{v}

- 1: **Input:** M_o , ρ , N_{mc} , ω , ϵ_c , \mathbf{v}
- 2: **Initialize:** $\mathbf{p}^{[0]} \in (0, 1)^M$ with $\sum_i p_i^{[0]} = M_o$ (e.g., uniform distribution), $t \leftarrow 0$
- 3: **repeat**
- 4: Draw $\zeta_n^{[t]} \sim \text{Bernoulli}(\mathbf{p}^{[t]})$ ($n = 1, \dots, N_{mc}$)
- 5: Compute $\{\bar{R}_S(\zeta_n^{[t]})\}_{n=1}^{N_{mc}}$ using \mathbf{v}
- 6: $\mathcal{E}^{[t]} \leftarrow$ indices of top- ρ samples by \bar{R}_S
- 7: Compute $\{\mu_i^{[t]}\}_{i=1}^M$ by (36)
- 8: Find the unique ν^\dagger from (39)
- 9: Update $\mathbf{p}^{[t+1]}$ by (40)
- 10: $t \leftarrow t + 1$
- 11: **until** $\|\mathbf{p}^{[t+1]} - \mathbf{p}^{[t]}\| < \epsilon_c$
- 12: $\hat{\mathcal{I}} \leftarrow$ top- M_o ($\mathbf{p}^{[t]}$) and form $\mathbf{S}_{M_o}^\dagger$ by $\hat{\mathcal{I}}$
- 13: **Output:** $\mathbf{S}_{M_o}^\dagger$

Theorem 3. Let $\nu \in \mathbb{R}$ be the Lagrange multiplier. The unique maximizer of (37) satisfies, for each i ,

$$\underbrace{\nu p_i^2 - (\nu + 1)p_i + \mu_i^{[t]}}_{\triangleq f(p_i, \nu)} = 0, \quad (38)$$

whose solution in $(0, 1)$ is

$$p_i(\nu) = \begin{cases} \mu_i^{[t]} & (\nu = 0) \\ \frac{(\nu + 1) - \sqrt{(\nu + 1)^2 - 4\nu\mu_i^{[t]}}}{2\nu} & (\nu \neq 0). \end{cases} \quad (39)$$

Moreover, the mapping $\nu \mapsto \sum_{i=1}^M p_i(\nu)$ is strictly decreasing and continuous on its domain. Hence there exists a unique ν^\dagger such that $\sum_i p_i(\nu^\dagger) = M_o$.

Proof. See Appendix C. \blacksquare

Given ν^\dagger , let $\mathbf{p}^{\text{CE}} \triangleq \mathbf{p}(\nu^\dagger)$ the exact maximizer of CEM in (37). A standard smoothed update is then

$$\mathbf{p}^{[t+1]} = (1 - \omega)\mathbf{p}^{[t]} + \omega\mathbf{p}^{\text{CE}} \quad (\omega \in (0, 1)), \quad (40)$$

which preserves the expected “ M_o -sum” budget exactly since $\sum_i p_i^{[t]} = \sum_i p_i(\nu^\dagger) = M_o$ and by linearity in (40), and improves Φ by following theorem.

Theorem 4. $\mathbf{p}^{\text{CE}} = \mathbf{p}(\nu^\dagger)$ strictly increases Φ unless $\mathbf{p}^{[t]}$ already solves (37). Moreover, for any $\omega \in (0, 1]$, the smoothed update (40) yields $\Phi(\mathbf{p}^{[t+1]}) \geq \Phi(\mathbf{p}^{[t]})$.

Proof. Strict concavity and uniqueness of the maximizer imply $\Phi(\mathbf{p}^{\text{CE}}) > \Phi(\mathbf{p}^{[t]})$ unless optimality holds at $\mathbf{p}^{[t]}$. For the smoothed step, $\mathbf{p}^{[t+1]} = (1 - \omega)\mathbf{p}^{[t]} + \omega\mathbf{p}^{\text{CE}}$ remains feasible due to the strict concavity, and the concavity of Φ gives $\Phi(\mathbf{p}^{[t+1]}) \geq (1 - \omega)\Phi(\mathbf{p}^{[t]}) + \omega\Phi(\mathbf{p}^{\text{CE}}) \geq \Phi(\mathbf{p}^{[t]})$, and the theorem follows. \blacksquare

The overall procedure is summarized in Algorithm 2, whose monotonicity and convergence is guaranteed by theories of CEM in [50]. After verifying that the proposed algorithm concentrates $\mathbf{p}^{[t]}$ to \mathbf{p}^\dagger , we finally choose $\hat{\mathcal{I}}$ by selecting the top- M_o indices of $\mathbf{p}^{[t]}$, and form the optimal $\mathbf{S}_{M_o}^\dagger$.

Algorithm 3 Overall AO Framework for \mathbf{S}_{M_o} and \mathbf{v}

- 1: **Initialize:** $\mathbf{v}^{(0)}$, $\mathbf{S}_{M_o}^{(0)}$, $t \leftarrow 0$
- 2: Compute $\bar{R}_S^{(0)}$ by (15)
- 3: **repeat**
- 4: Given $\mathbf{S}_{M_o}^{(t)}$, run Algorithm 1 to obtain $\mathbf{v}^{(t+1)}$
- 5: Given $\mathbf{v}^{(t+1)}$, run Algorithm 2 to obtain $\mathbf{S}_{M_o}^{(t+1)}$
- 6: $\bar{R}_S^{(t+1)} \leftarrow \frac{1}{S} \sum_{s=1}^S \log_2 (1 + \gamma_s(\mathbf{v}^{(t+1)}, \mathbf{S}_{M_o}^{(t+1)}))$
- 7: $t \leftarrow t + 1$
- 8: **until** $|\bar{R}_S^{(t+1)} - \bar{R}_S^{(t)}| < \epsilon_{\text{out}}$
- 9: **Output:** $\mathbf{v}^* \leftarrow \mathbf{v}^{(t)}$, $\mathbf{S}_{M_o}^* \leftarrow \mathbf{S}_{M_o}^{(t)}$, $\bar{R}_S^* \leftarrow \bar{R}_S^{(t)}$

C. Overall Procedure

The two subproblems in Section III-A and III-B are alternately solved until convergence:

$$\dots \rightarrow \mathbf{S}_{M_o}^{(t)} \rightarrow \mathbf{V}^{(t+1)} \rightarrow \mathbf{S}_{M_o}^{(t+1)} \rightarrow \dots, \quad (41)$$

where the overall procedure is given in Algorithm 3. Note that $\mathbf{v}^{(0)}$ is initialized according to Remark 1, while $\mathbf{S}_{M_o}^{(0)}$ is generated by randomly selecting M_o active ports from the M available candidates. This proposed AO framework effectively decouples the continuous reflection design and the discrete port-selection, while ensuring monotonic improvement of the overall objective.

D. Overall Convergence of Algorithm 3

We now combine the above results to discuss the convergence of the full AO procedure in Algorithm 3. Let $\bar{R}_S^{(t)}$ denote the SAA objective value in (15) evaluated at $(\mathbf{v}^{(t)}, \mathbf{S}_{M_o}^{(t)})$ in Algorithm 3. Then, for each outer iteration t :

- Given $\mathbf{S}_{M_o}^{(t)}$, Algorithm 1 produces $\mathbf{v}^{(t+1)}$ such that

$$\bar{R}_S(\mathbf{v}^{(t+1)}, \mathbf{S}_{M_o}^{(t)}) \geq \bar{R}_S(\mathbf{v}^{(t)}, \mathbf{S}_{M_o}^{(t)}), \quad (42)$$

due to the monotonicity property by Theorem 2

- Given $\mathbf{v}^{(t+1)}$ and sufficiently large N_{mc} , Algorithm 2 yields $\mathbf{S}_{M_o}^{(t+1)}$ which guarantees [50]

$$\bar{R}_S(\mathbf{v}^{(t+1)}, \mathbf{S}_{M_o}^{(t+1)}) \geq \bar{R}_S(\mathbf{v}^{(t+1)}, \mathbf{S}_{M_o}^{(t)}). \quad (43)$$

Therefore, the outer AO iterates generate a (deterministically or in expectation) non-decreasing sequence

$$\bar{R}_S^{(0)} \leq \bar{R}_S^{(1)} \leq \dots \leq \bar{R}_S^{(t)} \leq \dots \quad (44)$$

which is bounded above by the maximum achievable rate under the given power and hardware constraints. Consequently, $\{\bar{R}_S^{(t)}\}$ converges to a finite \bar{R}_S^* with its limit point $(\mathbf{v}^*, \mathbf{S}_{M_o}^*)$.

IV. COMPLEXITY ANALYSIS

We characterize the computational complexity of the proposed AO framework for FARIS by each step on Algorithm 3.

A. Complexity of SAA-Based Rate Evaluation

For fixed $(\mathbf{v}, \mathbf{S}_{M_o})$, the SAA objective \bar{R}_S in (15) requires to compute $\{\gamma_s\}$ in (18), which is dominated by each denominator term $\mathbf{v}^* \mathbf{C}_s \mathbf{v}$ with $\mathcal{O}(M_o^2)$ operations. Hence, the rate evaluation yields the complexity of $\mathcal{O}(SM_o^2)$.

B. Complexity of Algorithm 1

1) *Variable and Constraint Dimensions*: In order to characterize the computational complexity of the subproblem in (25), we explicitly define the dimensions of the optimization variables and the associated constraints:

$$n_{\text{var}} = M_o^2 + 2S, \quad n_{\text{cone}} = M_o^2 + 3S, \quad n_{\text{lin}} = M_o + 1 + 3S, \quad (45)$$

where n_{var} is the number of decision variables, n_{cone} is the total conic dimension, and n_{lin} is the number of linear inequality constraints.

2) *Interior-Point Complexity of Solving (25)*: A generic primal-dual interior-point step for mixed LMI/SOC problems incurs complexity of [48]

$$\mathcal{O}\left(n_{\text{var}}^3 + n_{\text{var}}^2 n_{\text{cone}} + n_{\text{var}} n_{\text{cone}}^2 + n_{\text{var}}^2 n_{\text{lin}}\right). \quad (46)$$

Substituting (45) to (46), the computational complexity Cost_{sub} of solving (25) with K_{IP} steps is given by

$$\begin{aligned} \mathcal{O}\left(K_{\text{IP}}\left((M_o^2 + 2S)^3 + (M_o^2 + 2S)^2(M_o^2 + 3S) \right. \right. \\ \left. \left. + (M_o^2 + 2S)(M_o^2 + 3S)^2 \right. \right. \\ \left. \left. + (M_o^2 + 2S)^2(M_o + 1 + 3S)\right)\right) \\ = \mathcal{O}(K_{\text{IP}}(M_o^2 + S)^3). \end{aligned} \quad (47)$$

3) *Gaussian Randomization*: The Cholesky factorization of \mathbf{V}_0 requires $\mathcal{O}(M_o^3)$ flops and is performed once [49]. For each randomized candidate, generating \mathbf{v}_n and evaluating the S quadratic terms $\text{tr}(\mathbf{C}_s \mathbf{V}_n)$ and $\text{tr}(\mathbf{a}_s \mathbf{a}_s^* \mathbf{V}_n)$ incur $\mathcal{O}(SM_o^2)$ operations. Furthermore, the reduced conic subproblem in $\{w_s, \xi_s\}$ satisfies $n_{\text{var}} = 2S$ and $n_{\text{cone}} = n_{\text{lin}} = 3S$; hence the arithmetic cost per interior-point iteration is $\mathcal{O}(K'_{\text{IP}}S^3)$ with K'_{IP} steps by (46). Consequently, the overall complexity of the Gaussian randomization stage is

$$\mathcal{O}(M_o^3 + N_{\text{rand}}(SM_o^2 + K'_{\text{IP}}S^3)), \quad (48)$$

and the element-wise magnitude projection requires $\mathcal{O}(M_o)$, which is negligible compared to the dominant terms.

4) *Auxiliary Update*: Updating y_s via (30) requires $\text{tr}(\mathbf{C}_s \mathbf{V})$ with complexity of $\mathcal{O}(SM_o^2)$.

Hence, the total complexity of Algorithm 1 with T_v iterations is given by

$$\text{Cost}_{\mathbf{v}\text{-update}} = \mathcal{O}\left(T_v(K_{\text{IP}}(M_o^2 + S)^3 + N_{\text{rand}}(SM_o^2 + K'_{\text{IP}}S^3))\right). \quad (49)$$

C. Complexity of Algorithm 2

1) *Sampling and Rate Evaluation*: At iteration t of Algorithm 2, we draw N_{mc} i.i.d. $\{\zeta_n^{[t]}\}$. Since generating one such vector requires M independent Bernoulli trials, the total sampling complexity is $\mathcal{O}(N_{\text{mc}}M)$.

For each $\zeta_n^{[t]}$, we evaluate $\{\bar{R}_S(\zeta_n^{[t]})\}_{n=1}^{N_{\text{mc}}}$. Thus, by the result in Section IV-A, the total complexity of evaluating all N_{mc} samples is $\mathcal{O}(N_{\text{mc}}SM_o^2)$.

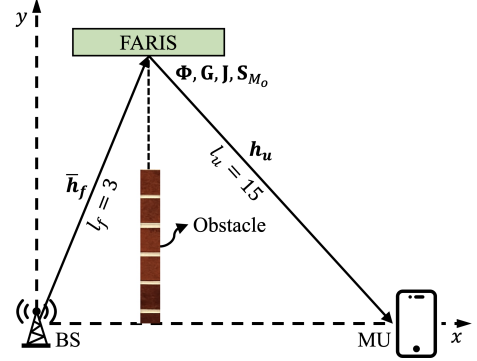


Fig. 2. Simulation setup of the FARIS-aided system.

2) *Elite Selection and Statistics*: Thereafter, we select the top- ρ fraction of samples as $\mathcal{E}^{[t]}$. Sorting the N_{mc} fitness values requires $\mathcal{O}(N_{\text{mc}} \log N_{\text{mc}})$, which is optimal for comparison-based sorting. Once $\mathcal{E}^{[t]}$ of size $\lceil \rho N_{\text{mc}} \rceil$ is determined, $\mu_i^{[t]}$ in (36) must be computed. Each $\mu_i^{[t]}$ requires summing the i th entries of N_e binary vectors of length M . Therefore, the overall complexity of computing all M components of $\mu^{[t]}$ is $\mathcal{O}(\rho N_{\text{mc}} M)$.

3) *Solving for ν^\dagger* : Each evaluation of $g(\nu)$ costs $\mathcal{O}(M)$, and bisection with L_ν steps gives $\mathcal{O}(L_\nu M)$.

Hence, the total complexity of Algorithm 2 with T_{CEM} iterations is given by

$$\begin{aligned} \text{Cost}_{\mathbf{S}\text{-update}} = \mathcal{O}\left(T_{\text{CEM}}(N_{\text{mc}}SM_o^2 + N_{\text{mc}}M + N_{\text{mc}} \log N_{\text{mc}} \right. \\ \left. + L_\nu M)\right). \end{aligned} \quad (50)$$

D. Overall AO Complexity

Combining the results, we get the total complexity of the proposed AO framework with T_{AO} iterations as

$$\text{Cost}_{\text{total}} = \mathcal{O}\left(T_{\text{AO}}\left(\text{Cost}_{\mathbf{v}\text{-update}} + \text{Cost}_{\mathbf{S}\text{-update}} + SM_o^2\right)\right). \quad (51)$$

V. SIMULATION RESULTS

In the simulations, we assess the effectiveness of the proposed AO frameworks for maximizing \bar{R} through Monte-Carlo evaluations. The FARIS setup, as shown in Fig. 2, considers a deployment of the BS, FARIS, and MU, with distances $l_f = 3$ m and $l_u = 15$ m. Since $l_f = 3$ m is smaller than $D^{\text{RB}} = 6$ m, the LoS condition for \bar{h}_f is satisfied [45]. The channels between the ARIS and MU are modeled as flat Rician fading channels, with a path-loss exponent of 2.2 and $K = 1$ [51], [52], and the detailed simulation parameters are listed in Table I. Each Monte-Carlo point is computed by averaging over 10^3 independent realizations of signal transmission and reception. For comparison, we also include the performance of (i) a conventional FRIS (passive) architecture with the same number of M_o FRIS elements selected from M candidates with the particle-swarm-optimization (PSO)-based

TABLE I
SIMULATION PARAMETERS

Parameter	Value
Number of FARIS/FRIS elements M (unless referred)	100 (10×10)
Maximum amplification gain g_{\max}	40 [dB] [12]
Reflection power budget of FARIS P_{\max}	25 [dBm] [12]
Transmit power P (unless referred)	15 [dBm]
Noise at FARIS and MU (σ_r^2, σ_0^2)	-90 [dBm] (same)
Normalized FARIS/FRIS aperture W_x (unless referred)	2
Parameters in CEM (N_{mc}, ρ, ω)	($5N, 0.1, 0.7$) [42], [50]

approach in [40], and (ii) an ARIS architecture with same M_o elements with sequential convex approximation (SCA)-based optimization in [12]. We additionally compare our results with a BFS baseline that exhaustively evaluates every possible port-phase configuration of the FRIS, assuming a $b = 2$ -bit discrete phase quantization and one-dimensional search over $[0, g_{\max}]$ [44].

Fig. 3 depicts the preset position candidates for the FARIS when employing $M_o = 16, 36$ and 81 fluid elements, which show the inherent flexibility of the FARIS architecture. For each case, the most advantageous $S_{M_o}^*$ is determined by CEM-based Algorithm 2. The resulting element selections exhibit a consistent tendency to activate elements located near the array boundary rather than those concentrated toward the center. This behavior can be physically explained by considering the effective aperture and spatial diversity of the FARIS. Elements placed farther from the array centroid experience larger angular separation and distinct incidence geometries, thereby offering lower inter-element correlation and contributing more significantly to the expansion of diversity and DoF through optimized \mathbf{G} .

Fig. 4 depicts the cumulative distribution function (CDF) of the ergodic-rate gap, together with that of the BFS benchmark, for $M = 16$ and $M_o \in \{4, 9\}$. Notably, the FARIS equipped with the proposed AO framework achieves near-optimal performance, closely tracking the exhaustive BFS curve despite the dramatic reduction in computational burden. The average gap remains as small as 0.53 and 0.75 bps/Hz for $M_o = 4$ and 9, respectively, a practically negligible loss considering that BFS requires evaluating the entire discrete port-phase space and optimal amplification control, whereas our method converges rapidly with orders-of-magnitude lower complexity. This highlights the efficiency and scalability of the proposed AO framework, even under stringent configuration constraints.

Fig. 5 illustrates the convergence behavior of $\bar{R}_S^{(t)}$ with the proposed AO framework for different values of M_o . The proposed algorithm shows a monotonic increase in the objective and typically converges within 15-20 iterations. The convergence speed is acceptable even though FARIS has more control variables (amplification + phase + port selection) than the FRIS baseline, demonstrating its practicality for real-time implementation in FARIS. Furthermore, as M_o increases, convergence becomes slightly slower due to the enlarged search space and stronger spatial correlation, which lessen the

marginal gain achieved at each iteration [53].

Fig. 6 presents \bar{R} versus P for FARIS and conventional FRIS/ARIS under $M_o = 16, 36$ and 81 . As P increases, FARIS with the proposed AO framework and ARIS initially exhibit a steeper rate growth; however, after certain threshold of P , the hardware constraint (9) in (13) becomes active, causing both curves to transition into a more moderate scaling with respect to P [12]. Consequently, the optimization gain of FARIS over ARIS also diminishes slightly in this high-power regime, as the ARIS amplification is limited by the same hardware bound. Nevertheless, FARIS still preserves a substantial rate margin over FRIS/ARIS, even with small M_o , as its fluid positioning and active amplification enable more effective exploitation of the aperture and yield sustained capacity gains over the counterparts; at $P = 25$ dBm, the FARIS with $M_o = 36$ and 81 yields 0.36 and 0.73 bps/Hz higher rate compared to ARIS architecture. Furthermore, with same $P = 25$ dBm, the FARIS configuration with $M_o = 16$ attains an average rate of approximately 8.02 bps/Hz, whereas the FRIS setup, despite employing a much larger aperture, achieves no more than 3.82 bps/Hz at $M_o = 81$, meaning that FARIS provides a 4.20 bps/Hz higher rate. This performance gap widens further for $M_o = 36$, making the rate of FARIS 5.14 bps/Hz higher. Moreover, increasing M_o improves \bar{R} for every architecture; however, the marginal gain decreases for larger M_o with fixed M , reflecting a saturation due to dense spatial sampling shown in Fig. 3.

Fig. 7 depicts the variation of \bar{R} with respect to M (or equivalently M_x) in the FARIS and conventional FRIS/ARIS configuration. For any fixed M , FARIS equipped with the proposed AO framework consistently achieves a higher rate than FRIS/ARIS, even with less M_o ; when $M_x = 16$, the proposed FARIS configuration with $M_o = 16$ provides an additional 3.66 bps/Hz over FRIS with $M_o = 81$, which increases to 4.33 bps/Hz when $M_o = 36$, and the gain over ARIS, whose fixed architecture yields a nearly flat rate profile due to the absence of extra DoFs or adaptive optimization, becomes readily apparent in the figure. This again highlights the substantial rate gain enabled by both fluid repositioning and active amplification. As M increases, both FARIS/FRIS architectures benefit from the denser aperture, which enhances spatial sampling and increases the likelihood of selecting more favorable element positions. Despite this common scaling benefit, FARIS maintains a clear performance margin over FRIS, as its fluid port placement together with active amplification enables more effective utilization of the expanded aperture, thereby providing rate enhancements unattainable by the purely passive counterpart.

Fig. 8 illustrates \bar{R} as a function of W_x for both FARIS and conventional FRIS. In the initial growth region, all schemes, including the proposed AO-enabled FARIS and the conventional FRIS, exhibit a sharp increase in \bar{R} due to the rapid reduction in spatial correlation and the improved ability to select favorable port positions as the aperture expands. This effect is also considerably pronounced for FARIS, similar to the previous observation, so that even a FARIS design with a smaller element count (e.g., $M_o = 16$) can surpass the rate of a larger-aperture FRIS configuration (e.g., $M_o = 36, 81$).

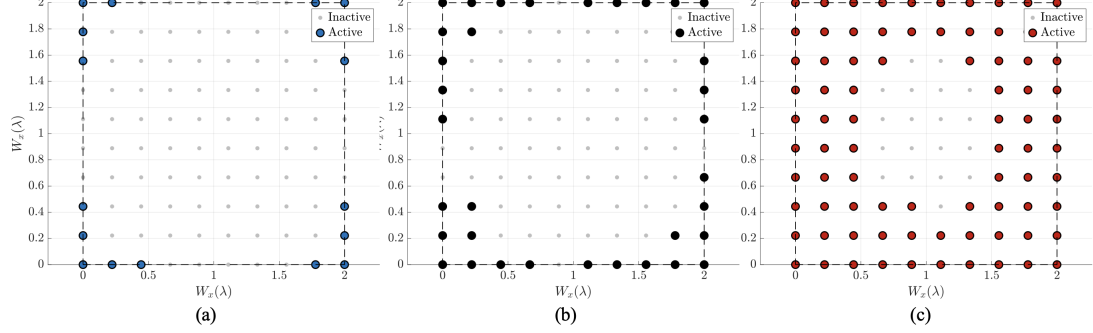


Fig. 3. Illustration of examples of the optimized positions when the FARIS has (a) $M_o = 16$ (b) $M_o = 36$ (c) $M_o = 81$ fluid active elements.

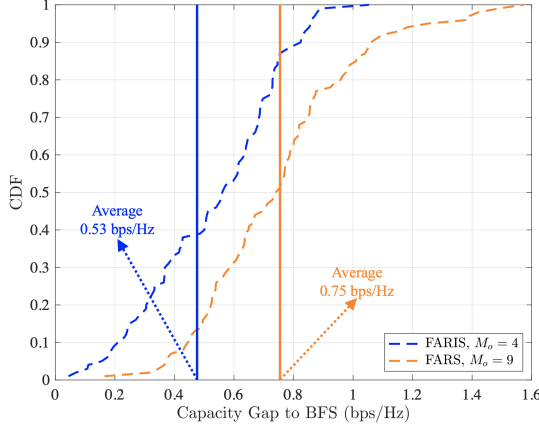


Fig. 4. CDF of ergodic rate gap between BFS and proposed AO frameworks for different M_o with $M = 16$.

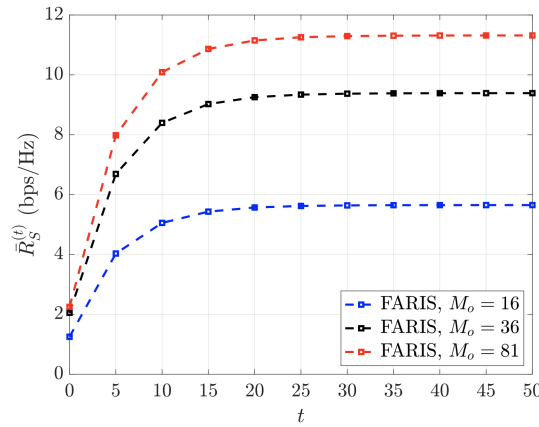


Fig. 5. Convergence performance of $\bar{R}_S^{(t)}$ by the proposed AO framework for different M_o .

As $W_x \gtrsim 5$, which corresponds to spacing of $\frac{\lambda}{2}$, the rate improvement begins to saturate since the additional aperture provides only marginal decorrelation benefits [29]. Notably, in this region, FARIS exploits the enlarged aperture far more effectively than FRIS, thanks to its jointly optimized fluid positioning and active amplification. Therein with $W_x = 6$, the rate difference between FARIS with $M_o = 16$ and FRIS

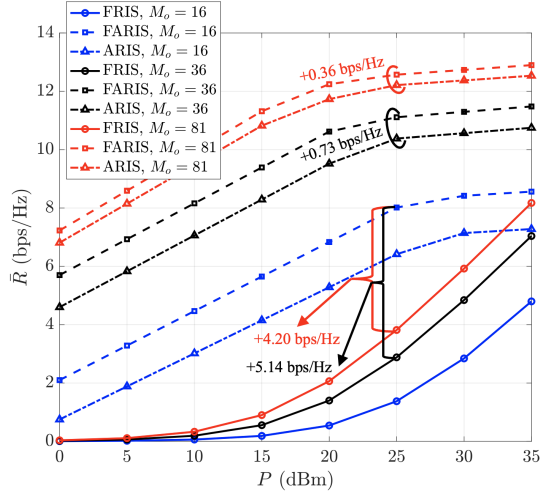


Fig. 6. Achievable rate \bar{R} versus Tx power P for different M_o FARIS/FRIS elements.

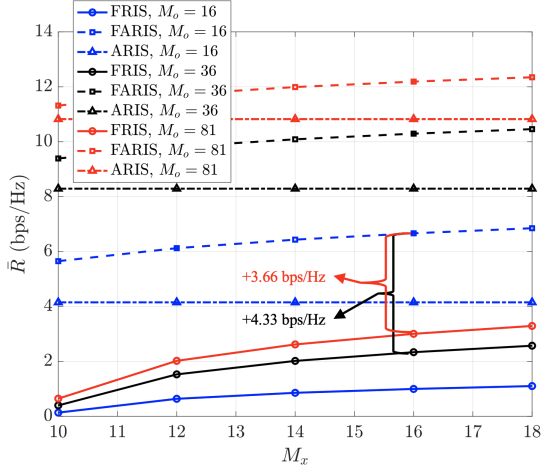


Fig. 7. Achievable rate \bar{R} versus the number of total elements M ($M_x \times M_x$) for different M_o FARIS/FRIS elements.

when $M_o = 81$ is 3.43 bps/Hz, which further widens to 3.90 bps/Hz when the number of active FRIS elements is reduced to $M_o = 36$. Although all schemes eventually show saturation after $W_x \gtrsim 5$, FARIS maintains a consistently larger

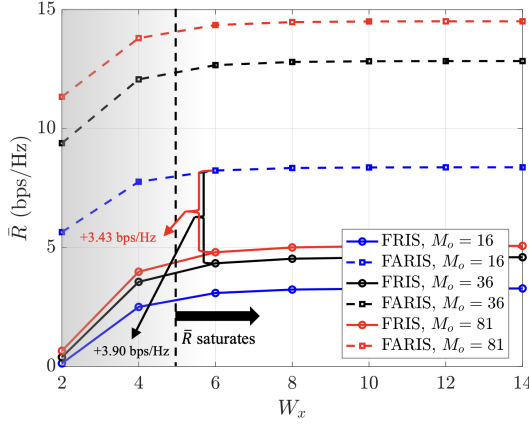


Fig. 8. Achievable rate \bar{R} versus normalized aperture W_x for different M_o FARIS/FRIS elements.

gain throughout the entire range of W_x .

VI. CONCLUSION

In this paper, we proposed the FARIS concept, a novel fluid-active-RIS architecture that jointly exploits fluid port repositioning and per-port amplification to substantially enhance the performance of RIS-aided wireless network. We developed a correlated FARIS channel model based on Jakes' spatial correlation and formulated an ergodic-rate maximization problem under a realistic reflection-power constraint, jointly optimizing active reflection coefficients and port selection. To tackle the resulting mixed-integer non-convex program, we introduced an AO framework that alternates between: i) a lifted active-reflection design solved via SAA and a quadratic-transform-based conic optimization in the lifted matrix variable, and ii) an M_o -constrained CEM-based port-selection scheme with a closed-form characterization guaranteeing a unique solution and monotonic improvement of the underlying likelihood. Simulation results showed that FARIS with proposed AO framework converges within a modest number of iterations and consistently outperforms a conventional FRIS/ARIS baseline across a wide range of transmit powers, total elements, and apertures, often achieving higher rates even with fewer active elements or smaller apertures. These findings demonstrate that combining fluid repositioning with active amplification provides a powerful additional DoF over FRIS/ARIS designs, positioning FARIS as a promising building block for 6G wireless environments.

APPENDIX A

PROOF OF THEOREM 1

We first prove (18). From (5) and (16),

$$\mathbf{h}^{(s)*} \mathbf{A}_{\text{act}} \tilde{\mathbf{h}}_f = \mathbf{u}_s^* \text{diag}(\mathbf{v}) \mathbf{b}, \quad (52)$$

and the square of magnitude becomes

$$|\mathbf{h}^{(s)*} \mathbf{A}_{\text{act}} \tilde{\mathbf{h}}_f|^2 = \mathbf{v}^* \mathbf{a}_s \mathbf{a}_s^* \mathbf{v} = |\mathbf{a}_s^* \mathbf{v}|^2, \quad (53)$$

which is the numerator of γ_s in (15). Thereafter, the ARIS-induced noise term satisfies

$$\begin{aligned} \mathbf{h}^{(s)*} \mathbf{A}_{\text{act}} \mathbf{A}_{\text{act}}^* \mathbf{h}^{(s)} &= \mathbf{u}_s^* \text{diag}(\mathbf{v}) \mathbf{K} \text{diag}(\mathbf{v}^*) \mathbf{u}_s \\ &= \mathbf{v}^* (\mathbf{K} \odot (\mathbf{u}_s \mathbf{u}_s^*)) \mathbf{v}, \end{aligned} \quad (54)$$

Thus by (53) and (54), the denominator of γ_s in (15) is

$$\sigma_r^2 + \mathbf{v}^* \mathbf{C}_s \mathbf{v} \quad (\mathbf{C}_s \triangleq L_u \sigma_r^2 (\mathbf{K} \odot (\mathbf{u}_s \mathbf{u}_s^*))), \quad (55)$$

and using $\mathbf{V} = \mathbf{v} \mathbf{v}^*$ and $\text{tr}(\mathbf{X} \mathbf{v} \mathbf{v}^*) = \mathbf{v}^* \mathbf{X} \mathbf{v}$, we obtain (18).

We now prove (19). Again by using (5) and (16),

$$\|\mathbf{A}_{\text{act}} \tilde{\mathbf{h}}_f\|_2^2 = \mathbf{v}^* \mathbf{Q}_1 \mathbf{v}, \quad (\mathbf{Q}_1 \triangleq \text{diag}(\mathbf{b}^*) \mathbf{K} \text{diag}(\mathbf{b}) = \mathbf{K} \odot (\bar{\mathbf{b}} \mathbf{b}^T)). \quad (56)$$

Similarly,

$$\begin{aligned} \text{tr}(\mathbf{A}_{\text{act}} \mathbf{A}_{\text{act}}^*) &= \text{tr}(\text{diag}(\mathbf{v}^*) \mathbf{K} \text{diag}(\mathbf{v}) \mathbf{K}) \\ &= \mathbf{v}^* \mathbf{Q}_2 \mathbf{v} \quad (\mathbf{Q}_2 \triangleq \mathbf{K} \odot \mathbf{K}). \end{aligned} \quad (57)$$

Therefore, by defining $\mathbf{F} \triangleq P_{\text{L}} \mathbf{Q}_1 + \sigma_r^2 \mathbf{Q}_2$, P_{RIS} becomes

$$P_{\text{RIS}} = \mathbf{v}^* \mathbf{F} \mathbf{v} = \text{tr}(\mathbf{F} \mathbf{V}), \quad (58)$$

and the theorem follows. \blacksquare

APPENDIX B

PROOF OF THEOREM 2

At iteration t of Algorithm 1, we assume that $(\mathbf{V}^{[t]}, \{y_s^{[t]}\}_{s=1}^S)$ has been obtained. By construction of the update rule in (30), the equality holds in the quadratic-transform lower-bound in (23) at $\mathbf{V}^{[t]}$, i.e.,

$$\bar{R}_S^{[t]} = \frac{1}{S} \sum_{s=1}^S \log_2(1 + \xi_s^{[t]}), \quad (59)$$

where $\xi_s^{[t]}$ denotes ξ_s evaluated at $(\mathbf{V}^{[t]}, \{y_s^{[t]}\})$. Fixing $\{y_s^{[t]}\}$, we solve (25) to obtain $\mathbf{V}^{[t+1]}$. Since $\mathbf{V}^{[t+1]}$ maximizes the lower-bound in (23) for fixed $\{y_s^{[t]}\}$, it holds that

$$\frac{1}{S} \sum_{s=1}^S \log_2(1 + \bar{\xi}_s^{[t+1]}) \geq \frac{1}{S} \sum_{s=1}^S \log_2(1 + \xi_s^{[t]}), \quad (60)$$

where $\bar{\xi}_s^{[t+1]}$ denotes ξ_s evaluated at $(\mathbf{V}^{[t+1]}, \{y_s^{[t]}\})$. Then $\{y_s^{[t+1]}\}$ are updated via (30), which is the unique maximizer of the quadratic-transform identity in (22). Therefore, the equality holds in the lower-bound in (23) at $\mathbf{V}^{[t+1]}$, i.e.,

$$\bar{R}_S^{[t+1]} = \frac{1}{S} \sum_{s=1}^S \log_2(1 + \xi_s^{[t+1]}) \geq \frac{1}{S} \sum_{s=1}^S \log_2(1 + \bar{\xi}_s^{[t+1]}). \quad (61)$$

Hence, by combining (59)-(61), we obtain

$$\bar{R}_S^{[t+1]} = \frac{1}{S} \sum_{s=1}^S \log_2(1 + \xi_s^{[t+1]}) \geq \frac{1}{S} \sum_{s=1}^S \log_2(1 + \xi_s^{[t]}) = \bar{R}_S^{[t]}. \quad (62)$$

Thus, $\{\bar{R}_S^{[t]}\}$ monotonically non-decreases, and the theorem follows. \blacksquare

APPENDIX C

PROOF OF THEOREM 3

The Lagrangian of (37) is

$$\mathcal{L}(\mathbf{p}, \nu) = \sum_i (\mu_i^{[t]} \log p_i + (1 - \mu_i^{[t]}) \log(1 - p_i)) + \nu(M_o - \sum_i p_i). \quad (63)$$

Stationarity yields $\frac{\mu_i^{[t]}}{p_i} - \frac{1 - \mu_i^{[t]}}{1 - p_i} - \nu = 0$, which rearranges to (38). For $\nu = 0$, $p_i = \mu_i^{[t]}$ holds. For $\nu \neq 0$, the quadratic condition in (38) admits two real roots since $\mu_i^{[t]} \in (0, 1)$:

$$p_i^{(\pm)}(\nu) = \frac{(\nu + 1) \pm \sqrt{(\nu + 1)^2 - 4\nu\mu_i^{[t]}}}{2\nu}, \quad (64)$$

which implies the following two scenarios:

- 1) $\nu > 0$: The product of $p_i^{(\pm)}(\nu)$ becomes $\frac{\mu_i^{[t]}}{\nu} > 0$, so the roots have same signs, and since $f(0, \nu) = \mu_i^{[t]} > 0$ and $f(1, \nu) = \mu_i^{[t]} - 1 < 0$, one root lies in $(0, 1)$ and the other in $(1, \infty)$. Because the denominator $2\nu > 0$, $p_i^{(+)} > p_i^{(-)}$ holds. Therefore, $p_i^{(+)} > 1$ while $p_i^{(-)} \in (0, 1)$.
- 2) $\nu < 0$: The product of $p_i^{(\pm)}(\nu)$ becomes $\frac{\mu_i^{[t]}}{\nu} < 0$, so the roots have opposite signs. Again, $f(0, \nu) = \mu_i^{[t]} > 0$ and $f(1, \nu) = \mu_i^{[t]} - 1 < 0$ imply that the positive root lies in $(0, 1)$ and the negative one is less than 0. Since the denominator $2\nu < 0$, $p_i^{(-)} > p_i^{(+)}$ holds. Therefore, $p_i^{(-)} \in (0, 1)$ still holds.

Hence, $p_i^{(-)}(\nu) \in (0, 1)$ holds for all $\nu \neq 0$, and we denote it simply by $p_i(\nu)$ as in (39).

To prove strictly decreasing, define $f(p_i, \nu) \triangleq \nu p_i^2 - (\nu + 1)p_i + \mu_i^{[t]} = 0$. By the implicit function theorem:

$$\frac{\partial p_i}{\partial \nu} = -\frac{\frac{\partial f_i}{\partial \nu}}{\frac{\partial f_i}{\partial p_i}} = -\frac{p_i^2 - p_i}{2\nu p_i - (\nu + 1)}. \quad (65)$$

Because $p_i \in (0, 1)$, we have $p_i^2 - p_i = p_i(p_i - 1) < 0$, so the numerator in (65) is negative. For denominator, by letting $\Delta \triangleq (\nu + 1)^2 - 4\nu\mu_i^{[t]}$, from (39) we have $2\nu p_i - (\nu + 1) = -\sqrt{\Delta} < 0$. Combining these signs gives

$$\frac{\partial p_i}{\partial \nu} = -\frac{(\text{negative})}{(\text{negative})} < 0, \quad (66)$$

which proves that $p_i(\nu)$ is strictly decreasing in ν .

Continuity of $p_i(\nu)$ follows directly from its closed-form expression in (39), which implies that $g(\nu) \triangleq \sum_i p_i(\nu)$ is also strictly decreasing and continuous. Moreover, as $\nu \rightarrow -\infty$ leads to $p_i(\nu) \rightarrow 1$ so $g(\nu) \rightarrow M$, and as $\nu \rightarrow +\infty$, $p_i(\nu) \rightarrow 0$, so $g(\nu) \rightarrow 0$. Hence by the intermediate value theorem, for any target $M_o \in (0, M)$, there exists a unique ν^* satisfying $g(\nu^*) = M_o$, and the theorem follows. ■

REFERENCES

- [1] Q. Wu *et al.*, "Intelligent reflecting surface-aided wireless communications: A tutorial," *IEEE Trans. Commun.*, vol. 69, no. 5, pp. 3313–3351, May 2021.
- [2] X. Mu *et al.*, "Reconfigurable intelligent surface-aided near-field communications for 6G: Opportunities and challenges," *IEEE Veh. Technol. Mag.*, vol. 19, no. 1, pp. 65–74, Mar. 2024.
- [3] T. Gong *et al.*, "Holographic MIMO communications: Theoretical foundations, enabling technologies, and future directions," *IEEE Commun. Surveys Tuts.*, vol. 26, no. 1, pp. 196–257, First quarter 2024.
- [4] D. Jun *et al.*, "Reconfigurable intelligence surface with potential tunable meta-devices for 6G: Design and system-level evaluation," *IEEE Commun. Stand. Mag.*, vol. 8, no. 4, pp. 32–39, Apr. 2024.
- [5] H.-B. Jeon *et al.*, "An energy-efficient aerial backhaul system with reconfigurable intelligent surface," *IEEE Trans. Wireless Commun.*, vol. 21, no. 8, pp. 6478–6494, Aug. 2022.
- [6] E. Björnson *et al.*, "Intelligent reflecting surface versus decode-and-forward: How large surfaces are needed to beat relaying?" *IEEE Wireless Commun. Lett.*, vol. 9, no. 2, pp. 244–248, Feb. 2020.
- [7] T. Y. Elgarni *et al.*, "STAR-RISs versus full-duplex decode-and-forward relaying: Which is better?" *IEEE Commun. Lett.*, vol. 29, no. 11, pp. 2556–2560, Nov. 2025.
- [8] M. Ahmed *et al.*, "Active reconfigurable intelligent surfaces: Expanding the frontiers of wireless communication-a survey," *IEEE Commun. Surveys Tuts.*, pp. 1–1, 2024.
- [9] Z. Zhang *et al.*, "Active RIS vs. passive RIS: Which will prevail in 6G?" *IEEE Trans. Commun.*, vol. 71, no. 3, pp. 1707–1725, Mar. 2023.
- [10] Q. Zhu *et al.*, "Joint beamforming designs for active reconfigurable intelligent surface: A sub-connected array architecture," *IEEE Trans. Commun.*, vol. 70, no. 11, pp. 7628–7643, Nov. 2022.
- [11] K. Zhi *et al.*, "Active RIS versus passive RIS: Which is superior with the same power budget?" *IEEE Commun. Lett.*, vol. 26, no. 5, pp. 1150–1154, May 2022.
- [12] R. Long *et al.*, "Active reconfigurable intelligent surface-aided wireless communications," *IEEE Trans. Wireless Commun.*, vol. 20, no. 8, pp. 4962–4975, Aug. 2021.
- [13] J. Yang *et al.*, "Robust transmission design for active RIS-aided systems," *IEEE Trans. Veh. Technol.*, vol. 74, no. 7, pp. 11591–11596, Jul. 2025.
- [14] G. Zhou *et al.*, "A framework for transmission design for active RIS-aided communication with partial CSI," *IEEE Trans. Wireless Commun.*, vol. 23, no. 1, pp. 305–320, Jan. 2024.
- [15] M. Di Renzo *et al.*, "Smart radio environments empowered by reconfigurable intelligent surfaces: How it works, state of research, and the road ahead," *IEEE J. Sel. Areas Commun.*, vol. 38, no. 11, pp. 2450–2525, Nov. 2020.
- [16] G. Alexopoulos *et al.*, "RIS-enabled smart wireless environments: deployment scenarios, network architecture, bandwidth and area of influence," *Eurasip Jour. Wireless Commun. and Netw.*, vol. 203, no. 1, p. 103, Oct. 2023.
- [17] E. Basar *et al.*, "Reconfigurable intelligent surfaces for 6G: Emerging hardware architectures, applications, and open challenges," *IEEE Veh. Technol. Mag.*, vol. 19, no. 3, pp. 27–47, Sep. 2024.
- [18] Y. Liu *et al.*, "Reconfigurable intelligent surface-aided multi-user networks: Interplay between NOMA and RIS," *IEEE Wireless Commun.*, vol. 29, no. 2, pp. 169–176, Apr. 2022.
- [19] H. V. Cheng and W. Yu, "Degree-of-freedom of modulating information in the phases of reconfigurable intelligent surface," *IEEE Trans. Inf. Theory*, vol. 70, no. 1, pp. 170–188, Jan. 2024.
- [20] T. Jiang and W. Yu, "Interference nulling using reconfigurable intelligent surface," *IEEE J. Sel. Areas Commun.*, vol. 40, no. 5, pp. 1392–1406, May 2022.
- [21] R. Su *et al.*, "Capacity enhancement for reconfigurable intelligent surface-aided wireless network: From regular array to irregular array," *IEEE Trans. Veh. Technol.*, vol. 72, no. 5, pp. 6392–6403, May 2023.
- [22] S. Kayraklik *et al.*, "Indoor measurements for RIS-aided communication: Practical phase shift optimization, coverage enhancement, and physical layer security," *IEEE Open J. Commun.*, vol. 5, pp. 1243–1255, 2024.
- [23] J. Wang *et al.*, "Reconfigurable intelligent surface: Power consumption modeling and practical measurement validation," *IEEE Trans. Commun.*, vol. 72, no. 9, pp. 5720–5734, Sep. 2024.
- [24] K.-K. Wong *et al.*, "Fluid antenna systems," *IEEE Trans. Wireless Commun.*, vol. 20, no. 3, pp. 1950–1962, Mar. 2021.
- [25] W. K. New *et al.*, "A tutorial on fluid antenna system for 6G networks: Encompassing communication theory, optimization methods and hardware designs," *IEEE Commun. Surveys Tuts.*, pp. 1–1, 2024.
- [26] N. Shlezinger *et al.*, "Dynamic metasurface antennas for 6G extreme massive MIMO communications," *IEEE Wireless Commun.*, vol. 28, no. 2, pp. 106–113, Apr. 2021.
- [27] J. Zhang *et al.*, "A novel pixel-based reconfigurable antenna applied in fluid antenna systems with high switching speed," *IEEE Open J. Antennas Propag.*, vol. 6, no. 1, pp. 212–228, Feb. 2025.

- [28] W. K. New *et al.*, “Fluid antenna system: New insights on outage probability and diversity gain,” *IEEE Trans. Wireless Commun.*, vol. 23, no. 1, pp. 128–140, Jan. 2024.
- [29] K. K. Wong *et al.*, “Performance limits of fluid antenna systems,” *IEEE Commun. Lett.*, vol. 24, no. 11, pp. 2469–2472, Nov. 2020.
- [30] W. K. New *et al.*, “An information-theoretic characterization of MIMO-FAS: Optimization, diversity-multiplexing tradeoff and q -outage capacity,” *IEEE Trans. Wireless Commun.*, vol. 23, no. 6, pp. 5541–5556, Jun. 2024.
- [31] ———, “Channel estimation and reconstruction in fluid antenna system: Oversampling is essential,” *IEEE Trans. Wireless Commun.*, vol. 24, no. 1, pp. 309–322, Jan. 2025.
- [32] H. Xu *et al.*, “Channel estimation for FAS-assisted multiuser mmWave systems,” *IEEE Commun. Lett.*, vol. 28, no. 3, pp. 632–636, Mar. 2024.
- [33] W. Kiat New *et al.*, “Channel estimation and reconstruction in fluid antenna system: Oversampling is essential,” *IEEE Trans. Wireless Commun.*, vol. 24, no. 1, pp. 309–322, Jan. 2025.
- [34] J. Yao *et al.*, “FAS-RIS communication: Model, analysis, and optimization,” *IEEE Trans. Veh. Technol.*, vol. 74, no. 6, pp. 9938–9943, Jun. 2025.
- [35] F. Ghadi *et al.*, “On performance of RIS-aided fluid antenna systems” *IEEE Wireless Commun. Lett.*, vol. 13, no. 8, pp. 2175–2179, Aug. 2024.
- [36] L. Zhou *et al.*, “Fluid antenna-assisted ISAC systems,” *IEEE Wireless Commun. Lett.*, vol. 13, no. 12, pp. 3533–3537, Dec. 2024.
- [37] F. R. Ghadi *et al.*, “Performance analysis of FAS-aided NOMA-ISAC: A backscattering scenario,” *IEEE Internet Things J.*, vol. 12, no. 23, pp. 51 326–51 340, Dec. 2025.
- [38] H. Xu *et al.*, “The future is fluid: Revolutionizing DOA estimation with sparse fluid antennas,” *arXiv:2508.10826*, 2025.
- [39] ———, “Fluid antenna enabled direction-of-arrival estimation under time-constrained mobility,” *arXiv:2508.10820*, 2025.
- [40] A. Saleem *et al.*, “A first look at the performance enhancement potential of fluid reconfigurable intelligent surface,” *arXiv:2502.17116v1*, 2025.
- [41] H. Xiao *et al.*, “From fixed to fluid: Unlocking the new potential with fluid RIS (FRIS),” *arXiv:2509.18899*, 2025.
- [42] X. Zhu *et al.*, “Fluid reconfigurable intelligent surface (FRIS) enabling secure wireless communications,” *arXiv:2511.15860*, 2025.
- [43] F. Ghadi *et al.*, “Performance analysis of wireless communication systems assisted by fluid reconfigurable intelligent surfaces,” *IEEE Wireless Commun. Lett.*, vol. 14, no. 12, pp. 3922–3926, Dec. 2025.
- [44] H. Xiao *et al.*, “Fluid reconfigurable intelligent surfaces: joint on-off selection and beamforming with discrete phase shifts,” *IEEE Wireless Commun. Lett.*, vol. 14, no. 10, pp. 3124–3128, Oct. 2025.
- [45] J. Lee and S. Hong, “Near-field LoS/NLoS channel estimation for RIS-aided MU-MIMO systems: Piece-wise low-rank approximation approach,” *IEEE Trans. Wireless Commun.*, vol. 24, no. 6, pp. 4781–4792, Jun. 2025.
- [46] Z.-Q. Luo *et al.*, “Semidefinite relaxation of quadratic optimization problems,” *IEEE Signal Process. Mag.*, vol. 27, no. 3, pp. 20–34, May 2010.
- [47] K. Shen and W. Yu, “Fractional programming for communication systems—Part I: Power control and beamforming,” *IEEE Trans. Signal Process.*, vol. 66, no. 10, pp. 2616–2630, May 2018.
- [48] S. Boyd and L. Vandenberghe, *Convex Optimization*. Cambridge, UK: Cambridge Univ. Press, 2004.
- [49] A. Osinsky *et al.*, “Regularization for cholesky decomposition in massive MIMO detection,” *IEEE Wireless Commun. Lett.*, vol. 12, no. 9, pp. 1603–1607, Sep. 2023.
- [50] R. Y. Rubinstein and D. P. Kroese, *The Cross-Entropy Method: A Unified Approach to Combinatorial Optimization, Monte-Carlo Simulation, and Machine Learning*. Springer, 2004.
- [51] J. Yao *et al.*, “A framework of FAS-RIS systems: Performance analysis and throughput optimization,” *arXiv:2407.08141v1*, 2024.
- [52] B. Wei *et al.*, “Active reconfigurable intelligent surface-aided over-the-air computation networks,” *IEEE Wireless Commun. Lett.*, vol. 13, no. 4, pp. 1148–1152, Apr. 2024.
- [53] W.-Y. Fu, “Accelerated high-dimensional global optimization: A particle swarm optimizer incorporating homogeneous learning and autophagy mechanisms,” *Inf. Sci.*, vol. 648, p. 119573, Nov. 2023.